Chemical nature of the anion antisite in dilute phosphide $GaAs_{1-x}P_x$ alloy grown at low temperature

T. Demonchaux,[1] K. K. Sossoe,[1,2] M. M. Dzagli,[2] J. P. Nys,[1] M. Berthe,[1] D. Troadec,[1] A. Addad,[3] M. Veillerot,[4] G. Patriarche,[5] H. J. von Bardeleben,[6] M. Schnedler,[7] C. Coinon,[1] I. Lefebvre,[1] M. A. Mohou,[2] D. Stiévenard,[1] J. F. Lampin,[1] Ph. Ebert,[7] X. Wallart,[1] and B. Grandidier[1,*]

[1]*Université Lille, CNRS, Centrale Lille, ISEN, Université Valenciennes, UMR 8520 - IEMN, F-59000 Lille, France*

[2]*Laboratoire de Physique des Composants à Semi-conducteurs (LPCS), Département de Physique, FDS, Université de Lomé, BP 1515 Lomé, Togo*

[3]*Laboratoire de Structure et Propriétés de l'Etat Solide, Université des Sciences et Technologies de Lille, 59655 Villeneuve d'Ascq, France*

[4]*Université Grenoble Alpes, F-38000 Grenoble, France, and CEA, LETI, MINATEC Campus, F-38054 Grenoble, France*

[5]*Centre de Nanosciences et de Nanotechnologies, CNRS, Université Paris-Sud, Université Paris-Saclay, C2N–Marcoussis, 91460, Marcoussis, France*

[6]*Sorbonne Université, CNRS, Institut des Nanosciences de Paris (INSP), 4 Place Jussieu, 75005 Paris, France*

[7]*Peter Grünberg Institut, Forschungszentrum Jülich GmbH, 52425 Jülich, Germany*

(Received 5 June 2018; published 16 October 2018)

While nonstoichiometric binary III-V compounds are known to contain group-V antisites, the growth of ternary alloys consisting of two group-V elements might give additional degrees of freedom in the chemical nature of these antisites. Using cross-sectional scanning tunneling microscopy (STM), we investigate low-temperature-grown dilute $GaAs_{1-x}P_x$ alloys. High concentrations of negatively charged point defects are found. Combined with transmission electron microscopy and pump-probe transient reflectivity, this study shows that the defects have a behavior similar to the group-V antisites. Further analyses with x-ray diffraction point to the preferential incorporation of arsenic antisites, consistent with *ab initio* calculations, that yield a formation energy 0.83 eV lower than for phosphorus antisites. Although the negative charge carried by the arsenic antisites in the STM images is shown to be induced by the proximity of the STM tip, the arsenic antisites are not randomly distributed in the alloy, providing insight into the evolution of their charge state during the growth.

DOI: 10.1103/PhysRevMaterials.2.104601

I. INTRODUCTION

Molecular beam epitaxy (MBE) is widely used for the epitaxial growth of III-V compounds. This technique has been essential to obtain ternary or quaternary alloys with intermediate lattice parameters and band gaps between those provided by binary compounds. Tuning these properties is commonly achieved by changing the fraction of the alloyed atoms in the material based on rules that proved their worth. For ternary alloys with two different group-III elements, the composition of the semiconductor is thermodynamically controlled and is predominantly governed by the input flux ratio of both elements. As to ternary alloys containing two different group-V elements, the composition is highly nonlinear with the fraction of the group-V incident flux ratio and it is usually tailored with the temperature of the substrate. Deviations from these rules of thumb exist [1], but all these deviations have so far been understood and included in thermodynamic analyses of the growth to successfully predict the composition of ternary alloys depending on the growth parameters.

While the MBE growth of III-V semiconductors usually yields stoichiometric material, since group-V elements stick to the surface only if group-III atoms are present, it has been made possible to grow nonstoichiometric binary compounds with high crystal quality by lowering the substrate temperature [2]. In this case, group-V elements are also incorporated on cation lattice sites, giving rise to group-V antisites [3–5]. Such a low-temperature growth regime has been much less investigated for ternary compounds [6–9] and it is an open question whether the excess of anion atoms incorporated on the cation sublattice follows the same fraction of group-V elements incorporated on the anion sublattice. Because antisites are known to introduce defect states in the band gap of materials that trap free charge carriers and pin the Fermi level, controlling their chemical nature and thus the energy of the defect states would provide an additional degree of freedom in the generation of electromagnetic waves with ternary III-V compounds in the terahertz frequency range [10–13]. An appropriate choice of the ratio of group-V elements could also help in tuning the strain of the epilayer due to the incorporation of excess group-V elements, allowing for the growth of layers with a wider range of critical thicknesses [14,15].

Here we address this fundamental question and study the chemical nature of the antisite in a nonstoichiometric ternary compound semiconductor that consists of a dilute phosphide $GaAs_{1-x}P_x$ alloy. This alloy is a prototype system, since the mismatch in bond stiffness, lattice constant, and orbital energy between GaAs and GaP is rather small. The incorporation of excess group-V elements is achieved by growing a dilute phosphide $GaAs_{1-x}P_x$ alloy with molecular beam epitaxy

*Corresponding author: bruno.grandidier@isen.iemn.univ-lille1.fr

at low temperatures ranging between 240 °C and 325 °C. From the direct visualization of the native defects with cross-sectional scanning tunneling microscopy (STM), we identify the majority of the point defects as antisites, despite characteristic features that depart from the ones encountered in previous STM studies [3,16–18]. In particular, the antisites are found to be negatively charged. Additional grounds for the identification of the point defects as antisites are provided by pump-probe transient reflectivity and the analyses of annealed samples with STM and transmission electron microscopy (TEM).

Characterization of the strain in as-grown and annealed samples by high-resolution x-ray diffraction reveals the formation of a dilute phosphide $GaAs_{1-x}P_x$ alloy that contains a high concentration of arsenic antisites (As_{Ga}). *Ab initio* calculations of the formation energy of arsenic antisites and phosphorus antisites (P_{Ga}) show a lower formation energy for As_{Ga}, supporting the incorporation of excess arsenic into the epilayer instead of phosphorus. Finally, the charge state of the antisites was investigated in the low-temperature-grown (LTG) layers. We show the key role of the tip-induced band bending and the temperature to account for the observation of negative charge states close to the cleaved (110) surface. Based on electron-paramagnetic-resonance (EPR) analyses of the samples and the study of the antisite distribution in the STM images, we are also able to trace back the charge state of the As_{Ga} antisites during their incorporation into the LTG layers.

II. EXPERIMENTAL AND THEORETICAL DETAILS

1.5-μm-thick LTG layers were grown on *n*-type GaAs (001) substrates (3×10^{18} cm^{-3}) by MBE. They were separated from the substrates by a 50-nm-thick GaAs buffer layer and a 100-nm-thick $Ga_{51}In_{49}P$ potential barrier used as a marker to locate the LTG layer in the STM experiment. During the formation of the LTG-GaAs layer, a small amount of P atoms was incorporated to obtain a dilute phosphide alloy. The concentration of P in all the samples that were prepared did not exceed 2.3×10^{20} cm^{-3}, thus corresponding to a ratio between P atoms and As atoms of $\sim 1\%$ or less. For all the samples, such a concentration was analyzed with secondary ion mass spectroscopy (SIMS) to provide elemental depth profiles along the [001] growth direction (see Fig. 1). Different growth temperatures (T_g) between 325 °C and 240 °C were used to change the excess of group-V elements during the formation of the LTG layers. For all samples, the growth temperature of the LTG layers was measured by band-edge absorption spectroscopy. After growth, the samples were cut in several pieces. Some of them were annealed. The rapid thermal annealing consisted of a temperature ramp set at 25 °C/s, a stabilization of the temperature (T_a) at 580 °C or 620 °C for 40 s, and a cooling to room temperature in 80 s. All these steps were performed under a flow rate of 250 sccm of diazene (N_2H_2).

For investigations by cross-sectional TEM, thin lamellae were cut from the samples by focused ion beam and deposited on TEM grids. A typical cross-sectional high-angle annular dark-field scanning transmission electron microscope (HAADF-STEM) shows the structure of interest

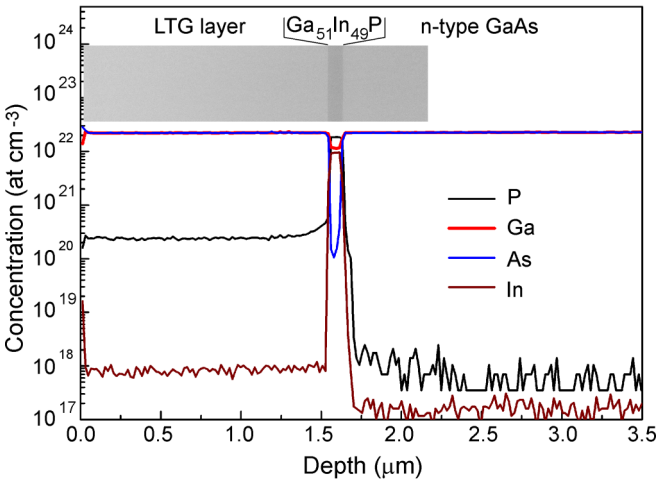

FIG. 1. SIMS concentration depth profiles of As, Ga, P, and In for a sample with a LTG layer grown at 240 °C. Inset: Cross-sectional HAADF-STEM image showing the basic structure of the sample.

(inset of Fig. 1). The samples were also characterized by cross-sectional STM on a clean cleavage surface. For optimal cleavage in ultrahigh vacuum (UHV), the samples were first thinned back to a thickness of 150 μm and then loaded into the UHV chamber. Directly after cleavage, the freshly exposed (110) surface of the samples was immediately examined with tungsten or platinum tips in a scanning tunneling microscope working at a temperature of 77 K. Tunneling spectroscopic measurements were performed at constant tip-sample separation to be compared with numerical simulations of the tunneling current. These simulations were based on the SEMITIP code [19], where the tip-induced band bending was calculated with a finite-element method assuming a hyperbolic-shaped probe tip. Due to the small concentration of phosphorus in the LTG layer, the semiconductor was considered as pure GaAs, treated in an effective-mass approximation, and tunnel currents were computed using the Bardeen method. The parameters in the computation were the tip radius-of-curvature, the tip-sample distance, the contact potential (difference between the work functions of the tip and the sample), and the doping level in the semiconductor. We note that all the STM and tunneling spectroscopic measurements reported in this manuscript were performed in the middle part of the 1.5-μm-thick LTG layer.

In order to measure the antisite concentration, the LTG layers were also studied by high-resolution x-ray diffraction. The incorporation of excess group-V atoms into the crystal results in lattice strain [4,20]. Therefore, the lattice parameters relative to the substrate were obtained from rocking curve measurements, where the diffraction peak from the LTG layers was compared to the Bragg maximum from the GaAs substrate to generate the splitting parameters $\Delta\theta$. The relative lattice parameter change $\Delta a/a$ induced by the antisites was deduced from $\Delta\theta$, taking into account the contribution due to the alloy composition. Such a contribution was obtained from the knowledge of the alloy composition on the basis of the SIMS profiles.

The EPR measurements were performed with a Bruker X-band spectrometer with standard field modulation at 100 kHz. The spectra were taken at $T = 4$ and 16 K, which are

the optimal temperatures for the observation of As_{Ga} antisites. Measurements were made with detached LTG layers, which were transferred on a Suprasil quartz plate in order to avoid the perturbation of the cavity quality factor by an *n*-type GaAs substrate. We equally studied layers deposited on a semi-insulating GaAs substrate. The $As_{Ga}{}^{+}$ spectrum was simulated with the EASYSPIN program, and the spin Hamiltonian parameters obtained are typical for EL2-like antisites.

Theoretical computations of the electronic structure were done within the density functional theory (DFT). Calculations were performed using the projector augmented wave (PAW) method [21,22], as implemented in the VASP code [23,24]. The Ga_{3d} electrons were treated as core electrons. For the bulk, the optimized cell parameter was obtained to be 5.606 Å, showing a deviation of 0.84% from the experimental value. In order to obtain the formation energies of the As and P antisites, $3 \times 3 \times 3$ supercells were used and consisted of 216 atoms. The cells were first relaxed while their size was kept fixed. The relaxation was computed with the Perdew-Burke-Ernzerhof (PBE) functional within the generalized gradient approximations (GGA) for the exchange and correlation energy [25]. A Monkhorst-Pack *k*-point mesh of (3 3 3) was employed. The electron wave function was expanded in plane waves up to a cut-off energy of 282.8 eV. The atomic positions were fully relaxed. The positions were optimized until the Hellmann-Feynman forces were less than 0.01 eV/Å. Then, as the computations of the formation energies of charged point defects require a good description of the band-gap energy, the fixed-structure hybrid correction (FSHC) was added to the PBE energy while applying the range-separated hybrid Heyd-Scuseria-Ernzerhof (HSE06) exchange-correlation functional to the PBE relaxed structure [26–28]. The HSE06 band gap of the bulk structure was computed to be 1.65 eV. To evaluate the formation energies of charged antisites, we made use of the method developed by Wu *et al.* [29]. This method aims at eliminating the difficulties associated with the long-range Coulomb interaction of charged defects. Considering that the cell remains electrically neutral, the defects become charged by trading electrons with bands: a positively charge defect comes with an electron in the conduction bands; conversely, a negatively charged defect comes with a hole in the valence band. Thus computations for charged defects were achieved with the indication of fulfilment of bands and the formation energies were calculated based on these rules.

Calculations of the electron density were performed by modeling the GaAs (110) surface in a supercell slab geometry consisting of four layers of GaAs in a 5×6 surface unit cell, including 240 Ga or As atoms. A vacuum region of 8.8 Å was used for all the calculations. In such a cell, the separation between a defect and its periodic image is sufficiently large to ensure negligible interaction. The bottom layer of the slab was passivated with pseudohydrogen (30 atoms H1.25 : $1s^{1.25}$ and 30 atoms H0.75 : $1s^{0.75}$) to saturate the dangling bonds [30]. The atomic positions were fully relaxed in all but the bottom layer. The electron density of the surface defects was computed for slab cells at the PBE level. In order to roughly mimic the STM experiments, the density of the highest occupied levels was integrated from the two topmost layers.

III. ATOMIC-SCALE IDENTIFICATION OF THE POINT DEFECTS

Figure 2 shows a typical cross-sectional STM image of the exposed (110) face of the LTG layer grown at 240 °C. Numerous bright features surrounded by a dark-ring-like depression that is superimposed to the atomic lattice appear in this high-resolution image. The presence of all these small features spread out on the surface is consistent with the high density of bulk point defects expected for a GaAs layer grown at low temperature. However, at first sight, most of the defects do not show the common characteristics of the subsurface As_{Ga} antisite, which consists of a central bright core and two weaker satellite peaks along the $[1\bar{1}2]$ and $[\bar{1}12]$ directions [3,16,17,18].

In order to identify these defects, we first analyze the electrical nature of the LTG layer at the local scale. The comparison of tunneling current spectra measured on the *n*-type GaAs (110) surface and on well-ordered areas of the LTG (110) surface shows a different electrical characteristic between both layers [Fig. 2(b)]. While a zero-current region extending over 1.5 V is measured on the *n*-type surface, with the Fermi level positioned close to the conduction band edge (E_C), we observe a larger apparent band gap on the LTG layer, with E_C shifted towards higher energies. The computation of the tunneling current for the *n*-type GaAs (110) surface shows good agreement with the experimental curve for a tip-sample separation of 0.55 nm, a tip radius of 40 nm, and a tip work function of 5.6 eV. In addition, we took into account the presence of a band of Ga dangling bond surface states, the so-called C_3 empty p_z-like dangling bond states, positioned 0.25 eV above the conduction band, that is found to limit the contribution of the tip-induced accumulation layer in the apparent band-gap region, consistent with previous work [19].

Assuming in first approximation a similar band structure for the dilute $GaAs_{1-x}P_x$ alloy and the pure GaAs as well as a low free carrier density in the LTG alloy ($1 \times 10^{16}\,cm^{-3}$), we were able to reproduce the increase of the tunneling current above +0.7 V and below −1.5 V, with a Fermi level position 0.5 eV below E_C at the $GaAs_{1-x}P_x$ cleavage surface. This Fermi energy is consistent with a lack of pinning in the bulk undoped LTG layer and a highly *n*-doped GaAs substrate [31], spilling some electrons into the undoped $GaAs_{1-x}P_x$ alloy. Despite such an electron spilling, the free carrier concentration is still low and leads to a large tip-induced band bending (TIBB). At negative sample voltages this TIBB drags the conduction band edge below the Fermi level. Hence, the bottom of the conduction band is populated with electrons; these electrons can tunnel from this accumulation zone first and, only at larger negative voltages do electrons tunnel from filled valence band states into the tip. This gives rise to the point of inflexion at −1.5 V [see red arrow in Fig. 2(b)].

This interpretation is supported directly by the corrugation observed in atomically resolved STM images measured at small magnitudes of negative voltages [see, e.g., inset in Fig. 2(b)]. The STM image exhibits atomic rows along the [001] direction, even though the atomic separation is smaller than the ones along the $[\bar{1}10]$ direction. This orientation of the corrugation morphology occurs only for the C_3 empty dangling bond state localized at the surface Ga atoms [32,33].

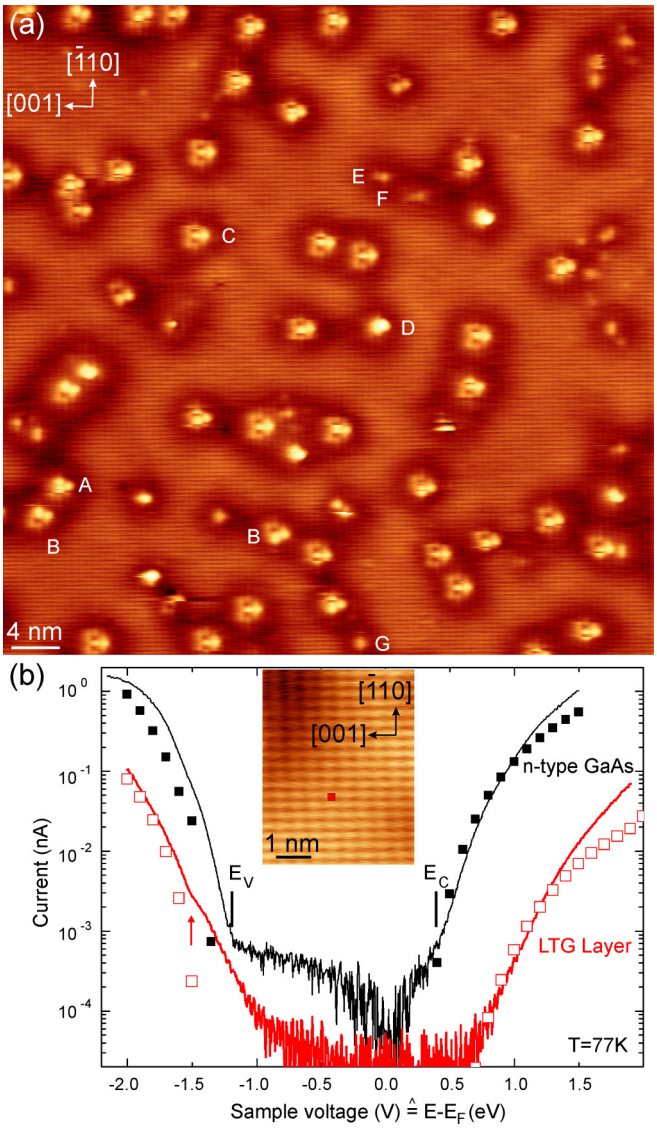

FIG. 2. (a) Constant-current STM image of the (110) cleaved face of the LTG layer grown at 240 °C (tunneling current $I_t = 10$ pA, sample voltage $V_S = -1.8$ V). The various defects are labeled as types A, B, C, D, E, F. (b) Tunneling spectra acquired from the n-doped GaAs substrate (upper curve) and the LTG layer grown at 240 °C (lower curve) ($I_t = 100$ pA, $V_S = +1.5\,\mathrm{V}/-2.0$ V). The valence band maximum E_V and conduction band minimum E_C are indicated by vertical segments. The arrow points to the onset of the valence band edge in the LTG layer. Filled and open squares show the theoretical computation for a high n-doped (3×10^{18} cm^{-3}) and low n-doped GaAs material (1×10^{16} cm^{-3}), respectively, taking into account the presence of a band of empty surface states at an energy of 0.25 eV above E_V. Inset: Occupied state STM image of the (110) cleaved face of the LTG layer free of point defects where the atomic corrugation is lower along than the [001] direction ($V_S = -1.8$ V). The corrugation pattern indicates tunneling from empty Ga derived dangling bonds, filled by the tip-induced downward band bending. The red square indicates the position of the spectrum measured on the LTG layer.

All other states lead to atomic rows along the [1̄10] direction. Hence, the tip probes at small magnitudes of negative voltage the Ga-derived C_3 dangling bond states resonant with the conduction band. This finding confirms the existence of a large TIBB that also shifts the valence band edge towards more negative voltages and leads to the large apparent band gap observed in the spectrum of the LTG layer. Moreover, it highlights the importance of the Ga dangling bond states in the tunneling process at negative sample voltages, when the tip scans a well-ordered area of the LTG layer.

In the vicinity of the point defect, the contrast changes, however. It becomes darker, with a predominant row orientation rotated by 90° from [001] to [1̄10] oriented rows. Such a depression reveals that the point defects are negatively charged. A negative charge center induces a local upward band bending, which prevents the tip-induced formation of the accumulation layer in the conduction band. In the constant-current mode, this effect results in a decrease of the tunneling current due to the localized absence of electrons in the conduction band, compensated by a reduction of the tip-to-sample distance to keep the current constant. Only the filled valence band states contribute to the tunneling current around the defects, accounting for a change of the row orientation. The observed vertical rows correspond to the A_5 dangling bond state localized at the anions (imaging of the anion sublattice).

Based on the identification of the atomic rows seen in the surrounding of the point defects, we now analyze the symmetry of the defect-related features. Figure 3 shows high-resolution STM images of three major types of defects that are found in Fig. 2(a). In Fig. 3(a), the type-A defect consists of three bright protrusions, a central one and two others pointing in [1$\bar{1}$2] and [$\bar{1}$12] directions. It is cut by a ($\bar{1}$10) mirror plane, shown as two dotted segments, that runs between two Ga rows. The central protrusion is thus located on a surface As sublattice row along the [001] direction. Moreover, the center of the triangle defined by the three protrusions is located between two surface As sublattice rows running along the [1$\bar{1}$0] direction. Such a position is consistent with a Ga site in the second atomic plane, taking the first plane as the surface [see Fig. 3(b)]. Therefore, we believe that this point defect is an anion antisite belonging to the second atomic plane. This is corroborated by the similarity of the contrast with the one theoretically predicted [34–36], despite the smaller size of its central core.

While the comparison of the atomic contrast for type-B and -C defects visible in Figs. 3(c) and 3(d) reveals some similarities with a type-A defect, both defects distinguish themselves by the contrast of their satellites. The satellites consist of either one protrusion and one atomic-sized depression (type-B defect) or two atomic-sized depressions (type-C defect). For the type-B defect, the protrusion and the depression can be found inverted with respect to the mirror plane. From the subsequent acquisition of sequential STM frames such as the one shown in Fig. 3(f), it is clear that the defects randomly switch from one type of defect to another type, sometimes with some intermediate configurations. For example, the central type-B defect in Fig. 3(f1) switches to a type-B' defect ($f2 \rightarrow f3$) that turns into a type-C defect ($f3 \rightarrow f4$). Then the type-C defect switches to a type-A defect ($f4 \rightarrow f5$). Based on these observations, we conclude that the defects seen in Figs. 3(b) and 3(c) correspond to an anion antisite in the second atomic plane and two anion third-neighbor surface As atoms in the [1$\bar{1}$2] and [$\bar{1}$12] directions that show strong

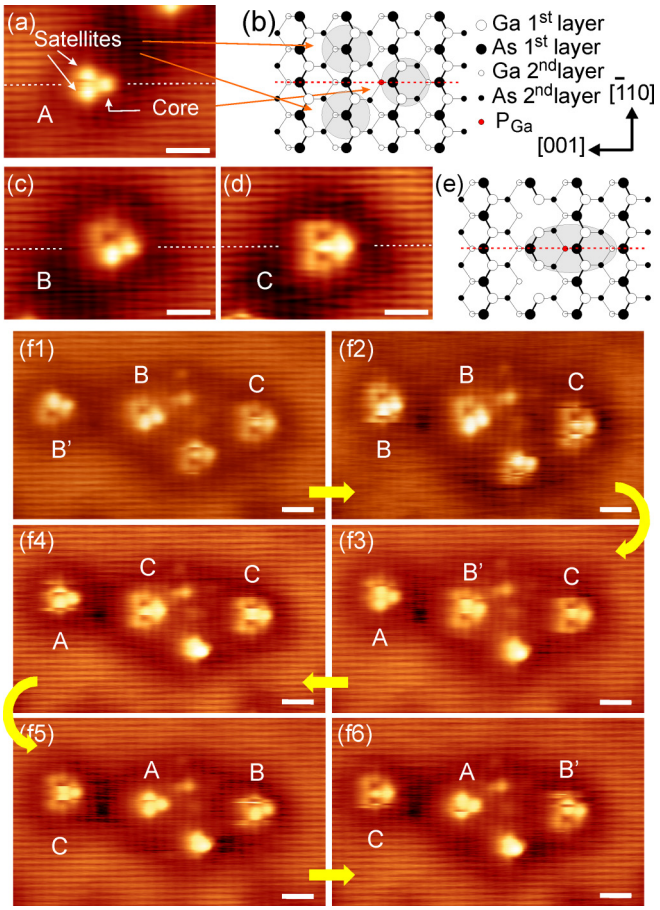

FIG. 3. Occupied state STM images of typical contrasts induced by defects in the (110) cleaved face of the LTG layer grown at 240 °C. The defect consists of (a) an antisite in the second layer, (b) an antisite in the second layer with a surface vacancy, (c) an antisite in the second layer with two surface vacancies ($I_t = 10$ pA, $V_S = -1.8$ V, scale bar: 2 nm). Schematic views of the surface showing the first and the second layers with (d) an antisite in the second layer and (e) an antisite in the second layer with two As vacancies in the next zigzag rows. $(1\bar{1}0)$ mirror planes are highlighted by horizontal dotted segments. (f) Sequence of successive STM images showing the evolution of the defect complexes that involve an antisite in the second layer and vacancies ($I_t = 10$ pA, $V_S = -1.8$ V, scale bar: 2 nm).

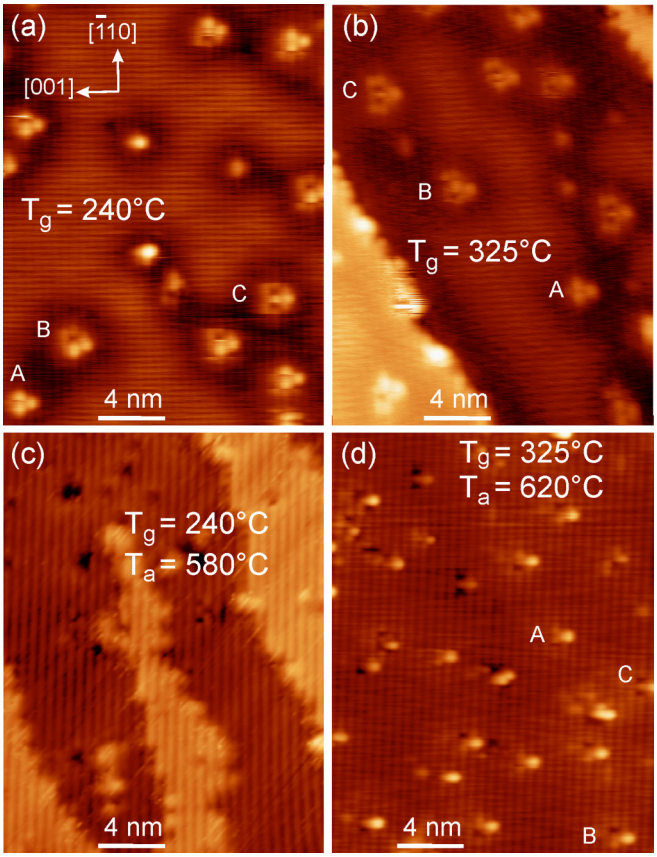

FIG. 4. Constant-current STM image of the (110) cleaved face of the LTG layers grown at a temperature (T_g) of (a) 240 °C and (b) 325 °C and respectively annealed at a temperature (T_a) of (c) 580 °C and (d) 620 °C. The bulk concentration of phosphorus in the LTG layers grown at 240 °C and 325 °C are 2.3×10^{20} cm^{-3} and 2.2×10^{20} cm^{-3}, respectively. Tunneling conditions: current of (a) 10 pA, (b) 10 pA, (c) 10 pA, (d) 5 pA; sample voltage of (a) −1.8 V, (b) −2.0 V, (c) −2.0 V, (d) −2.5 V. Antisites and antisite-vacancy complex belonging to the second atomic plane are labeled as types A, B, C.

instabilities. Counting the number of all these anion antisites, we find a corresponding bulk concentration of $7.1 \pm 0.2 \times 10^{19}$ cm^{-3} in the LTG layer grown at 240 °C, consistent with the high concentration of antisites usually encountered in LTG GaAs grown with the same temperature [3,37,38]. We note that all these defects are also visible in the LTG layer grown at 325 °C [Fig. 4(b)], albeit to a smaller concentration of $2.1 \pm 1.0 \times 10^{19}$ cm^{-3}, in agreement with the reduction of excess group-V atoms as the growth temperature increases [37].

In order to further check whether the point defects seen in the STM images behave similarly to the antisites, some of the samples were annealed prior to the cleavage. The LTG initially grown at 240 °C and annealed at 580 °C for 40 s exhibits no antisite anymore on its (110) cleavage surface [Fig. 4(c)]. Only dark depressions corresponding to single vacancies or clusters of vacancies are visible, along with the formation of numerous terraces. Their presence is consistent with the particular difficulty to cleave this type of sample [39]. The cross-sectional TEM analysis of the sample reveals many dark features with a mean diameter of 3.6 nm [Fig. 5]. They correspond to precipitates of group-V elements [2,38,40,41], the biggest ones giving rise to a Moiré fringe contrast (inset of Fig. 5), which is caused by a different crystal structure with respect to the LTG layer [42,43].

The existence of precipitates indicates the condensation of the point defects upon annealing. This process is expected for antisites [44]. Therefore, the disappearance of the point defects and the formation of precipitates support the identification of the point defects as antisites, although their STM contrast is slightly different from the one encountered in previous works [3,16,17,18]. We also note that, at the growth temperature of 325 °C, we were not able to find precipitates in the TEM images after annealing. Instead, the STM image of Fig. 4(d) shows a lot of point defects. Despite the

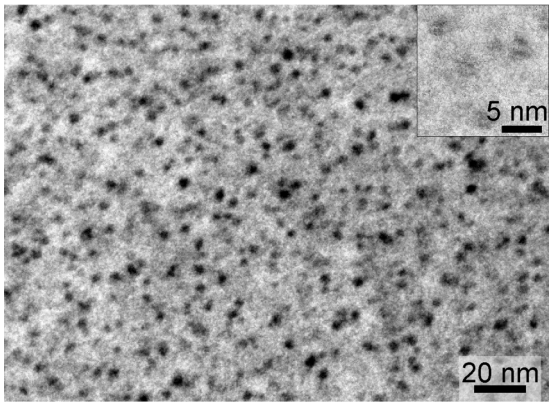

FIG. 5. Cross-sectional TEM micrograph of LTG layer grown at 240 °C and annealed at 580 °C for 40 s. Inset: High-magnification cross-sectional TEM micrograph revealing Moiré fringe contrast at the position of the biggest precipitates.

disappearance of the dark halo around the protrusions at a sample voltage of −2.5 V, the defects still have the same characteristic satellites, allowing us to categorize them as type-A, -B, and -C defects. All the defects consist of a bigger core. When both satellites are present, the type-A defect has the typical features of a subsurface antisite, confirming our conclusion.

An additional characteristic feature of the antisite is the short lifetime of the photoexcited carriers when III-V LTG materials contain a high concentration of antisites [2,45]. Pump-probe reflectivity measurements were thus performed for three LTG layers grown at temperatures of 240 °C, 260 °C, and 325 °C, respectively. As shown in Fig. 6, a dip is seen at the lowest growth temperature of 240 °C. It is caused by absorption processes due to the very high concentration of

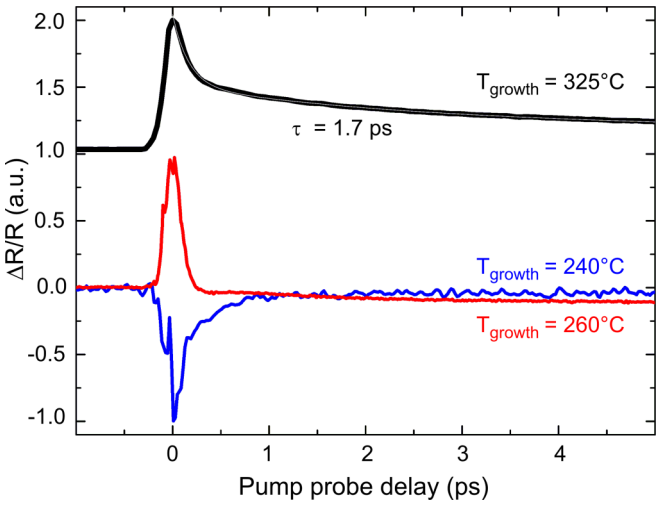

FIG. 6. Comparison of the normalized transient reflectivity of the LTG layers grown at 240 °C, 260 °C, and 325 °C. The corresponding concentrations of P atoms are 2.3×10^{20} cm^{-3}, 2.2×10^{20} cm^{-3}, and 1.5×10^{20} cm^{-3}. The thin solid line plotted for the LTG layer grown at 325 °C corresponds to the best fit of the curve by an exponential decay function with a time constant τ. The top spectrum has been shifted for clarity.

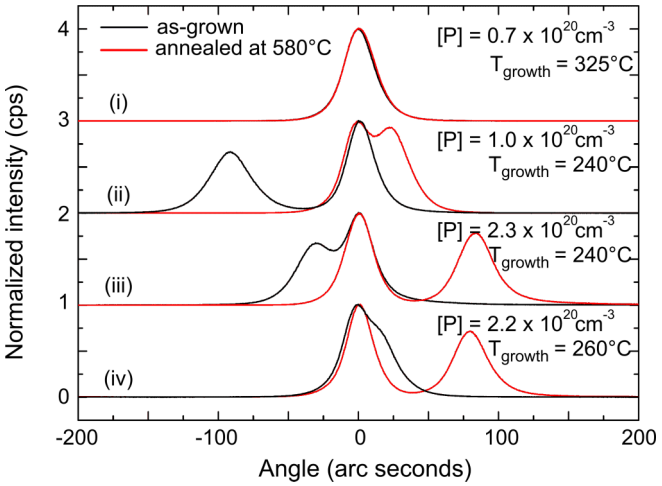

FIG. 7. Comparison of x-ray rocking curves measured for LTG layers grown at different temperatures and with different P contents before (as grown) and after annealing at 580 °C.

As_{Ga} antisites [46] and results in a very short lifetime, below the picosecond level. In contrast, at higher growth temperatures, the spectra exhibit an abrupt rise followed by a decrease of the signal. This decrease consists of a fast component at small pump-probe delay that is caused by the relaxation and cooling of the carriers in the bands. In the case of the sample grown at 325 °C, it is followed by a second component that can be fitted with an exponential decay, yielding lifetimes in the range of the picosecond. This increase of the lifetime with the growth temperature, and hence the decrease of the antisite concentration, is in agreement with the literature [47–50]. Due to the similarity of the lifetime found in the LTG layers with the ones given in the literature for LTG binary compounds, we believe that the majority of the point defects in the bulk have the physical characteristics of the antisites. But, at the surface, they appear in three different configurations A, B, and C, due to the instability of As atoms in their vicinity.

IV. CHEMICAL NATURE OF THE ANTISITE

In order to get insight into the chemical nature of the antisites, we performed x-ray diffraction (XRD) measurements, since this technique is able to detect the lattice expansion in a LTG layer with a significant excess of arsenic or phosphorus [4,51,52]. While the x-ray rocking curve for the LTG layer grown at the highest temperature of 325 °C and a phosphorus concentration of 0.7×10^{20} cm^{-3} yields a single peak in the spectrum (i) of Fig. 7, it shows two peaks for the LTG layer grown with a slightly higher P concentration and the lowest temperature of 240 °C (spectrum (ii) of Fig. 7). Based on the comparison of both spectra, the one centered at zero corresponds to the GaAs substrate. The other one centered at -93" reveals a strained layer that is attributed to the important excess of group-V elements in the LTG layer. As the concentration of phosphorus increases to 2.3×10^{20} P cm^{-3} [spectrum (iii) of Fig. 7], the peak shifts to -30", indicating a reduction of the strain in the epilayer.

This decrease could be caused by the existence of a tensile strain in the LTG layer when the concentration of phosphorus

atoms at anions sites increases [53]. But the shift could also arise from the incorporation of P_{Ga} antisites in the epilayer that would increase if their incorporation is preferred with respect to that of As_{Ga} antisites. Indeed, a P_{Ga} defect should induce a smaller dilated lattice distortion, since the tetrahedral covalent bond radius ($r = 1.06$ Å) of P is 12% smaller than that ($r = 1.19$ Å) of As [54]. DFT calculations of the bond lengths in a GaAs supercell containing either a P_{Ga} antisite or an As_{Ga} antisite confirm the change in bond radius mentioned above: a P_{Ga}-As bond has a length of $d_P = 2.49$ Å, that is smaller than an As_{Ga}-As bond, $d_{As} = 2.57$ Å. Such a bond length could lead to a smaller lattice expansion than the one obtained with the As antisites. In order to determine which hypothesis is valid, we analyzed a sample with a growth temperature of 260 °C and a P concentration of 2.2×10^{20} cm^{-3}. As seen in the spectrum (iv) of Fig. 7, the peak shifts to positive angles, corresponding to a lattice contraction in the epilayer. Since the decrease of the antisite concentration alone is not expected to give a peak at positive angle, such a shift is consistent with the growth of a $GaAs_{1-x}P_x$ alloy in tensile strain on the GaAs substrate. Therefore, this result favors the incorporation of As antisites rather than P antisites in the LTG layer.

Upon annealing, all the peaks are found at positive angles for the samples with P concentrations higher than 1.0×10^{20} cm^{-3}. According to the STM and TEM images shown above, the excess of group-V elements aggregates to form precipitates. As this process corresponds to a release of the strain, leading to the disappearance of the lattice mismatch in pure and annealed LTG-GaAs layers [38,55,56], the observation of a shoulder is consistent again with the growth of a $GaAs_{1-x}P_x$ LTG layer. Assuming that the majority of the P atoms are thus located on the anion sites of the lattice, the position of the peak at positive angles should provide a good indication of the concentration of P atoms in the layers. As this contraction takes place along the growth direction only, the relative contraction $(\Delta a/a)_{[001]}$, that is measured from the peak position in the XRD measurement, is related to the relative contraction of the relaxed lattice $(\Delta a/a)_r$ by

$$\left(\frac{\Delta a}{a}\right)_r = \frac{1-\nu}{1+\nu}\left(\frac{\Delta a}{a}\right)_{[001]}, \quad (1)$$

with $\nu = 0.31$ the Poisson coefficient for GaAs [57].

Based on Vegard's law, we deduce the ratio of P atoms from the relative expansion of the alloy with respect to the GaAs substrate:

$$\chi = -\frac{\left(\frac{1-\nu}{1+\nu}\right)\left(\frac{\Delta a}{a}\right)_{[001]} a_{GaAs}}{a_{GaAs} - a_{GaP}}. \quad (2)$$

For the LTG layers grown at 240 °C and 260 °C with the highest concentration of P atoms, the XRD measurements yield a phosphorus concentration of 2.0×10^{20} cm^{-3} for both samples. This concentration is in good agreement with the concentrations measured with SIMS and therefore indicates that the majority of the P atoms incorporated during the growth occupy the anion sites of the lattice.

Knowing the P concentration, we can relate the lattice expansion measured prior to the annealing to the concentration of As_{Ga} as follows:

$$\left(\frac{\Delta a}{a}\right)_{As_{Ga}[001]} = \left(\frac{\Delta a}{a}\right)_{BA[001]} - \left(\frac{\Delta a}{a}\right)_{AA[001]}, \quad (3)$$

where the subscripts BA and AA stand for before annealing and after annealing, respectively. On the basis of Ref. [37], we can finally deduce the concentration of the As antisites in the LTG layers:

$$[As_{Ga}] = 2.21 \times 10^{22} \frac{d_0^3}{d_{As}^3 - d_0^3}\left(\frac{\Delta a}{a}\right)_r. \quad (4)$$

We find an $[As_{Ga}]$ concentration of 5.3×10^{19} cm^{-3} for both samples grown at 240 °C with two different P concentrations. The concentration is of the same order of magnitude than the concentration obtained from the count of the As_{Ga} antisites at the cleavage surface of the same samples. This result indicates that the As atoms are preferentially incorporated as antisites rather than the P atoms.

In order to rationalize this experimental fact, a theoretical study of the formation energy of neutral, positively, and negatively charged As_{Ga} and P_{Ga} antisites was performed. Based on the method described above, the comparison of the formation energy between P_{Ga} and As_{Ga} was achieved by computing the chemical potentials of P and As atoms in respectively the phosphorus *Cmca* and the hexagonal As structure limits at the HSE06 level. As shown in Fig. 8, the neutral As_{Ga} antisite is found to be more stable than the neutral P_{Ga} antisite by 0.83 eV in GaAs bulk. As the Fermi level shifts to the valence band or the conduction band, the charge state of the antisites changes. This change occurs almost at the same energy for both As_{Ga} and P_{Ga} antisites, leading to a generally lower formation energy for As_{Ga} antisites with respect to P_{Ga} antisites, whatever the charge state is. Therefore, the theoretical calculation supports the incorporation of As_{Ga} antisites in a LTG dilute phosphide $GaAs_{1-x}P_x$ alloy, consistent with the conclusion drawn from the XRD analysis.

A further hint for the preferential incorporation of As atoms as antisites is obtained by calculating the electron density in the vicinity of an As_{Ga} or P_{Ga} antisite located in the second layer (first subsurface atomic plane) of a GaAs (110) surface. As shown in Fig. 9, the electron density calculated for the neutral As_{Ga} and P_{Ga} antisites is consistent with previous

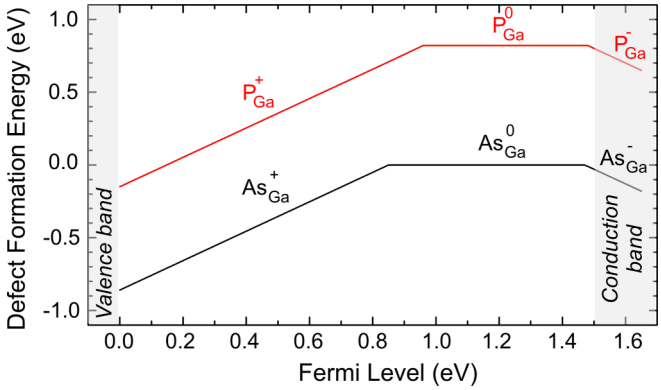

FIG. 8. Formation energy of the As_{Ga} and P_{Ga} antisites in bulk GaAs as a function of the Fermi level.

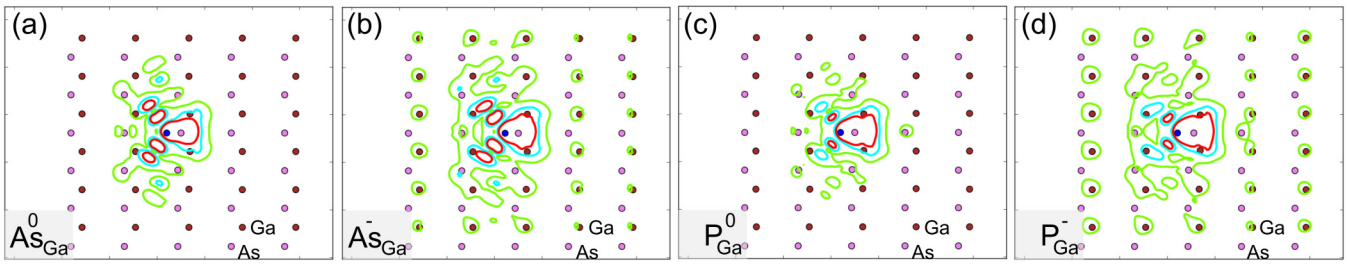

FIG. 9. Isosurfaces of the integrated electron density of the highest occupied levels of the (a) neutral and (b) negatively charged As_{Ga} as well as (c) neutral and (d) negatively charged P_{Ga} antisites located in the second layer (first subsurface atomic plane).

theoretical calculations [34,35,36], revealing a high electron density at the position of the antisite and along the $[1\bar{1}2]$ and $[\bar{1}12]$ directions. These areas correspond respectively to the core and the satellites of the antisites seen in the STM images. Interestingly, the P_{Ga} antisites show a reduced distribution of the electron density at the position of the satellites, no matter what the charge state is. Such a result suggests that the contrast of the satellites for the P_{Ga} antisites should be weak in the experimental STM images, opposite to the contrast observed for the antisites seen in Figs. 2–4.

V. CHARGE STATES OF THE ANTISITE

So far, most of the STM images have revealed a depression around the As_{Ga} antisites, meaning that the antisites carry a negative charge opposite to the neutral or positively charged state found in previous cross-sectional STM characterizations of pure GaAs LTG layers [3,16,17,18]. Although the existence of a negative charge state has been predicted [58], it has never been demonstrated experimentally and its observation casts doubt about the exact nature of the defects seen in the STM images. Therefore, the EPR technique was applied to the sample grown at 240 °C with a P concentration of $2.3 \times 10^{20}\,cm^{-3}$ to determine the charge state of the As_{Ga} antisites in the bulk of the LTG $GaAs_{1-x}P_x$ layer. Figure 10 compares the EPR spectrum measured for this sample with the spectrum of a semi-insulating GaAs substrate that is known to host a low concentration of As_{Ga} antisites. The spectrum measured in the LTG dilute phosphide $GaAs_{1-x}P_x$ alloy is almost flat, in clear contrast with the four lines typically detected in semi-insulating GaAs. These four lines are fitted using typical values for the Lande factor g, the hyperfine constant A, and the linewidth LW of each component of the quadruplet for the antisites [59] and are therefore the signature of singly positively charged As_{Ga} antisites in pure GaAs LTG layer [60]. We used equally different optical excitations (890–1200 nm) in order to increase the concentration of positively charged antisites, which are the paramagnetic species. But we did not observe any photoinduced effect on the LTG layer. As our sample contains a concentration of As_{Ga} antisites that is high enough to give a signal, the absence of the peaks indicates that the As_{Ga} antisites are neutral. This result is consistent with a Fermi level positioned in the upper part of the band gap, as already deduced by tunneling spectroscopy. Therefore, we attribute the observation of the negatively charged As_{Ga} antisites in STM images to the proximity of the surface.

Based on the tunneling spectroscopy and the simulation of the tunneling current discussed above, it has been concluded that a strong TIBB exists when the tip scans the LTG layer. At negative sample voltages, the band bending causes the formation of an electron accumulation layer at the surface that is directly visible through the observation of conduction band states (i.e., Ga-derived dangling bonds) in the high-resolution STM images of the occupied states. The strong downward TIBB at negative voltages also shifts the As_{Ga} antisite charge transition level (0/-) close to the conduction band edge below the Fermi level. As a result, the proximity of the polarized STM tip changes the charge state of the As_{Ga} antisite at the surface: a neutral antisite becoming negatively charged. This is compatible with the observed charge state in Fig. 2(a).

However, at present it remains unclear why a clear signature of a downward band bending is not always observed [see, e.g., Fig. 4(d)] and was not observed in prior studies of LT-GaAs by STM. As we discuss in the following, this is primarily an effect of using large negative set voltages, which shifts the dominating contribution of the tunnel current from the electron accumulation zone in the conduction band towards the filled valence band states. In order to illustrate this, the band bending was calculated and the respective band diagrams

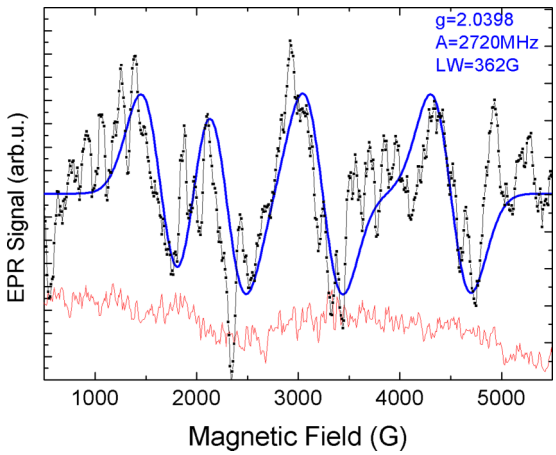

FIG. 10. Experimental EPR spectrum of the LTG layer grown at 240 °C with a P concentration of $2.3 \times 10^{20}\,cm^{-3}$ (lower curve) compared with the experimental and simulated (upper curves) EPR spectra of a LTG layer grown on a semi-insulating GaAs substrate. The simulation parameters that correspond to the electronic Lande factor g, the hyperfine constant A, and the linewidth LW are indicated in the graph.

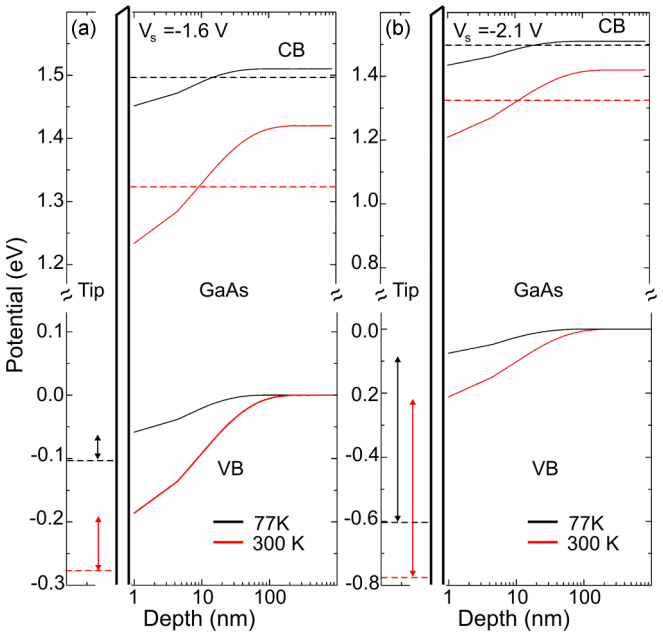

FIG. 11. Band diagrams of the metal-vacuum-LTG layer interface at two different temperatures for a sample voltage of (a) −1.6 V and (b) −2.1 V. The tip-induced band bending was calculated with the SEMITIP code [66], assuming a doping level of $1 \times 10^{16}\,\mathrm{cm}^{-3}$, a tip radius of 36 nm, a tip work function of 5.6 eV, a tip-sample distance of 6 Å, and a band of surface states related to the Ga dangling bonds positioned at an energy of 0.25 eV above E_C. The conduction and valence bands are labeled CB and VB, respectively. The dashed lines indicate the positions of the Fermi level in the tip (left) and in the LTG layer (right). The vertical arrows highlight the width of the valence band that contributes to the tunneling current in addition to the contribution of the occupied states in the conduction band.

were derived at temperatures of 77 and 300 K for different voltages (Fig. 11). The band diagrams show that the number of states in the electron accumulation zone in the conduction band changes only weakly with the magnitude of applied sample voltage. In contrast, the situation is fundamentally different for the valence band states contributing to the tunnel current: the number of valence band states increases drastically from a sample voltage of −1.6 to −2.1 V, whatever the temperature is. Hence, with increasing magnitude of negative voltages, the weight of the valence band states in the tunnel current dominates and the depression zone around negative charge centers weakens as it arises from spatial changes of the tunneling out of the electron accumulation zone in the conduction band. Ultimately, no signature of a charge will be detectable. This explains the absence of a depression in the STM image of Fig. 4(d), which was acquired at −2.5 V. It highlights the key role of the sample voltage to slightly change the contrast of the defects. These findings allow us to reconcile our observations with the STM image of Ref. [18] for a pure GaAs LTG layer grown on an *n*-type GaAs substrate and imaged at 77 K, where no depression was observed around the antisites.

It is interesting to note that the use of a *n*-type substrate makes the Fermi level unpinned in the bulk LTG layer. As the sample temperature gets lower, the Fermi level shifts to the conduction band edge. This shift corresponds to a band-gap broadening, leading to a reduction of the valence band states contributing to the tunneling current for a small sample voltage [Fig. 11(a)]. This effect thus favors the observation of a depression at low temperatures for an LTG layer grown on an *n*-type substrate. It also explains why the negatively charged antisites have never been observed for *p*-type LTG layers [3,16], since the Fermi level is pinned midgap in these layers [31], precluding the formation of an electron accumulation layer.

The negative charge carried by the antisite results from the shift of the transition level (0/-) below the Fermi level due to TIBB. It implies a transition level (0/-) close to the conduction band edge that is consistent with the theoretical predictions described above and the formation of a tip-induced potential well with limited spatial extent [61] that decouples the antisite state from the continuum of states in the conduction band. The negative charge is also seen for deeper As_{Ga} antisite defects, labeled D, E, and F in Fig. 2. Based on symmetry considerations with respect to the cation sublattice, they are attributed to antisites in the 3rd, 4th, and 5th atomic planes. Hence, the potential well extends a few atomic planes below the surface. Deeper, in the bulk, the transition level (0/-) stays above the Fermi level and all the bulk antisites are neutral, in agreement with the EPR measurements.

Remarkably, the antisites form a complex with one or two vacancies at the surface, as shown in Fig. 2(a). Based on the isosurfaces of the electron density for an antisite positioned in the second layer, it appears that a negative charge implies the partial filling of the closest Ga dangling bonds in the $[1\bar{1}2]$ and $[\bar{1}12]$ directions. This change of the electron distribution might weaken the As-Ga bonds at the surface. When the tip scans above the As surface atoms, the subsequent electronic excitation of the weakened bonds might favor the desorption of the atoms through a two-hole localization mechanism, for example [62,63], leaving a vacancy behind. If an As adatom sticks to the tip apex instead of binding with other free As atoms and desorbing as molecules, it could be further released during the next scans to replace a vacancy, giving rise to the switching behavior observed in Fig. 3. The negatively charged state of the antisite would therefore explain the formation of complex defects at the surface that was not reported in previous studies of the As_{Ga} with STM.

Finally, we notice the absence of close pairs of antisites in Fig. 2. This suggests a repulsive short-range interaction. As the antisites are not seen to diffuse after the cleavage, this interaction must have been occurring during incorporation into the LTG layer, already. A quantification of this repulsive interaction is obtained by collecting the position of the antisites in STM images and calculating the distances r between all possible pairs of antisites. This operation leads to the measured probability distribution of pair distances. Dividing this quantity by the pair distances for noninteracting randomly distributed antisites yields the two-dimensional pair correlation $c(r)$ [64], shown as an inset in Fig. 12. One can recognize a region in the center around 8 nm in diameter, where the contrast indicates a low pair probability. This indicates a repulsive interaction. The pair interaction energy can be approximated in the low-density limit by the mean

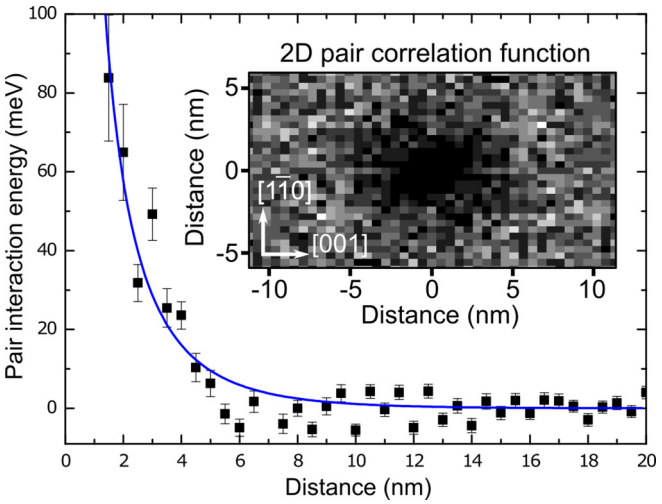

FIG. 12. Radial pair interaction energy derived from the pair-correlation function (inset) deduced from the spatial position of the antisites in STM images. The solid blue line is a fit of a three-dimensional bulk screened Coulomb potential model near the growth surface (i.e., with surface dielectric constant, see text). The data points to a $+1e$ charged state of the antisites during incorporation at the (001) growth surface.

force potential $W(r) = -kT\ln(c(r))$. The radially integrated pair interaction energy is plotted in Fig. 12 versus the radial separation r. It decreases exponentially as a function of the separation between the antisites, showing the existence of a repulsive interaction between the antisites.

At this stage we discuss the origin of the repulsion. We fitted different Coulomb interaction models to the data. The best fit is shown as blue line in Fig. 12. It is a screened Coulomb potential for three-dimensional bulk screening, modified by a surface dielectric constant. This result indicates that the antisites are charged near the growth surface, during their incorporation. At the GaAs (001) surface, the Fermi level is known to be pinned midgap [65]. Figure 8 indicates that the $(+/0)$ charge transition level is located above the Fermi energy, when the Fermi level is positioned at midgap. Hence, the antisite defects are positively charged during incorporation in the LTG layer at the growth surface. With progressing growth and hence increasing distance from the growth surface, the conduction band approaches the Fermi level due to the use of n-type GaAs substrate, and thereby the antisites become uncharged. This neutral charge state is consistent with the result obtained by EPR. The repulsive interaction that is seen in the STM images is thus reminiscent of the positive charge state of the antisites at the time of the growth. But during their observation in STM images the antisites are negatively charged due to the proximity of the STM tip.

VI. CONCLUSION

In summary, we have used complimentary techniques to identify the nature of point defects incorporated in low-temperature grown dilute phosphide $GaAs_{1-x}P_x$ alloys. We show that the excess of group-V elements gives rise to a preferential incorporation of As_{Ga} instead of P_{Ga}, while P is incorporated substitutional on anion sites. Based on the STM analysis of the LTG layers, we identify three different charge states for the As_{Ga} antisites: they are positively charged at the (001) growth surface, uncharged in the bulk LTG layer, and negatively charged at the (110) surface in the presence of positively biased STM tip. Furthermore, we observe a tip-induced bond rupture in the direct vicinity of the antisites at two specific lattice positions creating As vacancy–As_{Ga} antisite complexes. The weak bond strength at these positions is in contrast to antisites in pure LTG GaAs and could be related to the presence of P impurities.

Despite a change of the composition from pure GaAs to a dilute phosphide $GaAs_{1-x}P_x$ alloy, the critical physical properties of the As_{Ga} antisites in the $GaAs_{1-x}P_x$ matrix are kept identical: they give rise to subpicosecond carrier lifetimes and they condensate into precipitates upon annealing. Hence, LTG $GaAs_{1-x}P_x$ alloys are even preferable, since they reduce the strain in the epilayer while keeping the same amount of excess arsenic in comparison with pure LTG GaAs. Thus, LTG $GaAs_{1-x}P_x$ offers the advantage to reach higher critical thicknesses. This result also shows that the growth of a $Ga_{51}In_{49}P$ buffer layers in device fabrication is not detrimental to the electronic properties of a subsequently LTG GaAs contaminated with residual phosphorus atoms.

ACKNOWLEDGMENTS

This study was financially supported by the DGA (Direction Générale de l'Armement), the RENATECH network, the French National Research Agency (the Equipex Programs Excelsior, Grant No. ANR-11-EQPX-0015), and the Agence Universitaire de la Francophonie (Grant No. BAO-2012-05-52220FT2E0). The authors thank C. Delerue for useful discussions.

[1] D. M. Wood and A. Zunger, Phys. Rev. B **40**, 4062 (1989).
[2] M. R. Melloch, J. M. Woodall, E. S. Harmon, N. Otsuka, F. H. Pollak, D. D. Nolte, R. M. Feenstra, and M. A. Lutz, Annu. Rev. Mater. Sci. **25**, 547 (1995).
[3] R. M. Feenstra, J. M. Woodall, and G. D. Pettit, Phys. Rev. Lett. **71**, 1176 (1993).
[4] Y. He, N. A. El-Masry, J. Ramdani, S. M. Bedair, T. L. McCormick, R. J. Nemanich, and E. R. Weber, Appl. Phys. Lett. **65**, 1671 (1994).
[5] A. Díaz Álvarez, T. Xu, G. Tütüncüoglu, T. Demonchaux, J.-P. Nys, M. Berthe, F. Matteini, H. A. Potts, D. Troadec, G. Patriarche, J.-F. Lampin, C. Coinon, A. Fontcuberta i Morral, R. E. Dunin-Borkowski, P. Ebert, and B. Grandidier, Nano Lett. **15**, 6440 (2015).
[6] J. Sigmund, C. Sydlo, H. L. Hartnagel, N. Benker, H. Fuess, F. Rutz, T. Kleine-Ostmann, and M. Koch, Appl. Phys. Lett. **87**, 252103 (2005).
[7] X. Wallart, C. Coinon, S. Plissard, S. Godey, O. Offranc, Y. Androussi, V. Mangin, and J. F. Lampin, Appl. Phys. Express **3**, 111202 (2010).
[8] B. Globisch, R. J. B. Dietz, S. Nellen, T. Göbel, and M. Schell, AIP Adv. **6**, 125011 (2016).

[9] S. Zhou, M. Qi, L. Ai, S. Wang, A. Xu, and Q. Guo, J. Appl. Phys. **56**, 035505 (2017).

[10] A. Jooshesh, V. Bahrami-Yekta, J. Zhang, T. Tiedje, T. E. Darcie, and R. A. Gordon, Nano Lett. **15**, 8306 (2015).

[11] Y. Wang, I. Kostakis, D. Saeedkia, and M. Missous, IET Optoelectron. **11**, 53 (2016).

[12] M. Currie, in *Photodetectors: Materials, Devices and Applications*, edited by B. Nabet (Woodhead/Elsevier, Oxford, UK, 2016), pp. 121–155.

[13] D. R. Bacon, A. D. Burnett, M. Swithenbank, C. Russell, L. Li, C. D. Wood, J. Cunningham, E. H. Linfield, A. G. Davies, P. Dean, and J. R. Freeman, Opt. Exp. **24**, 26986 (2016).

[14] D. J. Eaglesham, L. N. Pfeiffer, K. W. West, and D. R. Dykaar, Appl. Phys. Lett. **58**, 65 (1991).

[15] K. G. Eyink, M. A. Capano, S. D. Walck, T. W. Haas, and B. G. Streetman, J. Electron. Mater. **26**, 391 (1997).

[16] B. Grandidier, H. Chen, R. M. Feenstra, D. T. McInturff, P. W. Juodawlkis, and S. E. Ralph, Appl. Phys. Lett. **74**, 1439 (1999).

[17] A. Hida, Y. Mera, and K. Maeda, Physica B **308–310**, 738 (2001).

[18] A. Hida, Y. Mera, and K. Maeda, Physica B **340–342**, 299 (2003).

[19] N. Ishida, K. Sueoka, and R. M. Feenstra, Phys. Rev. B **80**, 075320 (2009).

[20] M. Kaminska, E. R. Weber, Z. Liliental-Weber, R. Leon, and Z. U. Rek, J. Vac. Sci. Technol. B **7**, 710 (1989).

[21] P. E. Blöchl, Phys. Rev. B **50**, 17953 (1994).

[22] G. Kresse and D. Joubert, Phys. Rev. B **59**, 1758 (1999).

[23] G. Kresse and J. Furthmüller, Comput. Mat. Sci. **6**, 15 (1996).

[24] G. Kresse and J. Furthmüller, Phys. Rev. B **54**, 11169 (1996).

[25] J. P. Perdew, K. Burke, and M. Ernzerhof, Phys. Rev. Lett. **77**, 3865 (1996); **78**, 1396(E) (1997).

[26] L. Sponza, J. Goniakowski, and C. Noguera, Phys. Rev. B **91**, 075126 (2015).

[27] S. Heyd, G. E. Scuseria, and M. Ernzerhof, J. Chem. Phys. **118**, 8207 (2003).

[28] A. V. Krukau, O. A. Vydrov, A. F. Izmaylov, and G. E. Scuseria, J. Chem. Phys. **125**, 224106 (2006).

[29] Y. N. Wu, X. G. Zhang, and S. T. Pantelides, Phys. Rev. Lett. **119**, 105501 (2017).

[30] K. Shiraishi, J. Phys. Soc. Jpn. **59**, 3455 (1990).

[31] A. C. Warren, J. M. Woodall, P. D. Kirchner, X. Yin, F. Pollak, M. R. Melloch, N. Otsuka, and K. Mahalingam, Phys. Rev. B **46**, 4617 (1992).

[32] Ph. Ebert, B. Engels, P. Richard, K. Schroeder, S. Blügel, C. Domke, M. Heinrich, and K. Urban, Phys. Rev. Lett. **77**, 2997 (1996).

[33] Ph. Ebert, Surf. Sci. Rep. **33**, 121 (1999).

[34] R. B. Capaz, K. Cho, and J. D. Joannopoulos, Phys. Rev. Lett. **75**, 1811 (1995).

[35] S. B. Zhang, Phys. Rev. B **60**, 4462 (1999).

[36] Y. Iguchi, T. Fujiwara, A. Hida, and K. Maeda, Phys. Rev. B **71**, 125328 (2005).

[37] X. Liu, A. Prasad, J. Nishio, E. R. Weber, Z. Liliental-Weber, and W. Walukiewicz, Appl. Phys. Lett. **67**, 279 (1995).

[38] I. S. Gregory, C. M. Tey, A. G. Cullis, M. J. Evans, H. E. Beere, and I. Farrer, Phys. Rev. B **73**, 195201 (2006).

[39] R. M. Feenstra, A. Vaterlaus, J. M. Woodall, and G. D. Pettit, Appl. Phys. Lett. **63**, 2528 (1993).

[40] M. R. Melloch, N. Otsuka, J. M. Woodall, A. C. Warren, and J. L. Freeouf, Appl. Phys. Lett. **57**, 1531 (1990).

[41] P. A. Loukakos, C. Kalpouzos, I. E. Perakis, Z. Hatzopoulos, M. Sfendourakis, G. Kostantinidis, and C. Fotakis, J. Appl. Phys. **91**, 9863 (2002).

[42] M. Luysberg, H. Sohn, A. Prasad, P. Specht, Z. Lilienthal-Weber, E. R. Weber, J. Gebauer, and R. Krause-Rehberg, J. Appl. Phys. **83**, 561 (1998).

[43] V. V. Chaldyshev, Mater. Sci. Eng. B **88**, 195 (2002).

[44] D. E. Bliss, W. Walukiewicz, and E. E. Haller, J. Electron. Mater. **22**, 1401 (1993).

[45] Y. Terada, S. Yoshida, O. Takeuchi, and H. Shigekawa, Nat. Photon. **4**, 869 (2010).

[46] S. D. Benjamin, H. S. Loka, A. Othonos, and P. W. E. Smith, Appl. Phys. Lett. **68**, 2544 (1996).

[47] A. J. Lochtefeld, M. R. Melloch, J. C. P. Chang, and E. S. Harmon, Appl. Phys. Lett. **69**, 1465 (1996).

[48] S. S. Prabhu, S. E. Ralph, M. R. Melloch, and E. S. Harmon, Appl. Phys. Lett. **70**, 2419 (1997).

[49] M. Stellmacher, J. Nagle, J.-F. Lampin, P. Santoro, J. Vaneecloo, and A. Alexandrou, J. Appl. Phys. **88**, 6026 (2000).

[50] V. K. Mag-usara, S. Funkner, G. Niehues, E. A. Prieto, M. H. Balgos, A. Somintac, E. Estacio, A. Salvador, K. Yamamoto, M. Hase, and M. Tani, Opt. Exp. **24**, 26175 (2016).

[51] R. J. Matyi, M. R. Melloch, and J. M. Woodall, Appl. Phys. Lett. **60**, 2642 (1992).

[52] M. Fatemi, B. Tadayon, M. E. Twigg, and H. B. Dietrich, Phys. Rev. B **48**, 8911 (1993).

[53] A. Y. Lew, C. H. Yan, C. W. Tu, and E. T. Yu, Appl. Phys. Lett. **67**, 932 (1995).

[54] J. C. Phillips, *Bonds and Bands in Semiconductors* (Academic, New York, 1973), Chap. 1.

[55] M. Kaminska, Z. Liliental-Weber, E. R. Weber, T. George, J. B. Kortright, F. W. Smith, B-Y. Tsaur, and A. R. Calawa, Appl. Phys. Lett. **54**, 1881 (1989).

[56] S. Fleischer, C. D. Beling, S. Fung, W. R. Nieveen, J. E. Squire, J. Q. Zheng, and M. Missous, J. Appl. Phys. **81**, 190 (1997).

[57] J. S. Blakemore, J. Appl. Phys. **53**, R123(R) (1982).

[58] D. J. Chadi, Phys. Rev. B **68**, 193204 (2003).

[59] A. Goltzene, B. Meyer, C. Schwab, S. G. Greenbaum, R. J. Wagner, and T. A. Kennedy, J. Appl. Phys. **56**, 3394 (1984).

[60] H. J. von Bardeleben, M. O. Manasreh, D. C. Look, K. R. Evans, and C. E. Stutz, Phys. Rev. B **45**, 3372 (1992).

[61] R. Dombrowski, Chr. Steinebach, Chr. Wittneven, M. Morgenstern, and R. Wiesendanger, Phys. Rev. B **59**, 8043 (1999).

[62] K. Tanimura, Phys. Rev. B **69**, 033301 (2004).

[63] J. Tssuruta, E. Inami, J. Kanasaki, and K. Tanimura, Surf. Sci. **626**, 49 (2014).

[64] Ph. Ebert, T. Zhang, F. Kluge, M. Simon, Z. Zhang, and K. Urban, Phys. Rev. Lett. **83**, 757 (1999).

[65] M. D. Pashley, K. W. Haberern, R. M. Feenstra, and P. D. Kirchner, Phys. Rev. B **48**, 4612 (1993).

[66] R. M. Feenstra, J. Vac. Sci. Technol. B **21**, 2080 (2003).